https://doi.org/10.5194/amt-2022-69
Preprint. Discussion started: 25 April 2022

Atmospheric Measurement Techniques Discussions
Open Access

Performance evaluation of an integrated path differential absorption LIDAR model for surface pressure from low-Earth orbit

Guanglie Hong [1], Yu Dong [2], Huige Di [2]

[1]Shanghai Institute of Technical Physics, Chinese Academy of Sciences, Shanghai, 200083, China
[2]Xi 'an University of Technology, Xi 'an,710048, China

Correspondence to: Dong Yu (dy_raister@163.com), Di Huige (dihuige@xaut.edu.cn)

Abstract. Remote sensing of surface pressure from space is critical; differential absorption LIDAR and differential absorption radar are only two kinds of remote sensing instruments with this potential. The differential absorption LIDAR works in integral path mode from the satellite in low-Earth orbit. It measures the differential optical depth of the Oxygen A-band, and the surface pressure is thereafter obtained by performing circle-iterative calculation. Performance evaluation of the differential absorption LIDAR model was conducted with respect to the advanced system parameters of the space instrument, Low echo pulse energy at ocean surface and the challenging calculation of repetitive cumulative average of echo on uneven land surface yielded random errors in surface pressure measurement. On the other hand, uncertain atmospheric temperature and water vapor mixture profiles resulted in systematic error of surface pressure. Consequently, controlling the error of surface pressure within 0.1% proved challenging. Under a strict implementation of the error budget, the time resolution is 6.25 s and along-orbit distance resolution is 44km, and the results showed that 765.6735/765.4637 nm is suitable as the working wavelength pair. Further, error could be expected to within 0.2–0.3% for the cumulative average of 625 ocean surface laser pulse echoes, cumulative average of more than 144 pulse echoes on land, and observation from the 400km orbit.

1 Introduction

Atmospheric pressure plays a vital role in several atmospheric processes related to atmospheric dynamics. Low/high pressure, low pressure troughs, high pressure ridges, and anticyclones and other related information have been introduced into the atmospheric model. Hurricanes are profound low-pressure systems that originate from low-pressure cyclones in the tropical or subtropical oceanic regions. Accurate prediction of their formation, landing direction, and movement trajectory requires atmospheric pressure gradient distribution data. Fundamentally, the density of the atmosphere in high latitudes increase during winter, causing the air to shrink and sink, thereby increasing the pressure and gradually resulting in the formation of a powerful, deep, and broad air mass. Upon the accumulation of a sufficient cold high-pressure force, a cold wave is formed, which rolls out and pours down. Meanwhile, airspace for the release of radio sounding balloons is restricted; thus, continuous detection during the entire day is not possible. Brown et al.(1986) reported that the accuracy of the weather models is primarily limited by the regional sparsity of the input data. Specifically, atmospheric pressure data is very sparse in large areas of the ocean, desert, plateaus, and polar regions. Consequently, the International Meteorological Organization aims to achieve remote sensing of surface pressure at an accuracy of 0.1–0.3%(Korb et al., 1995)(WMO-ICSU, 1973), which however, remains a big challenge.

https://doi.org/10.5194/amt-2022-69
Preprint. Discussion started: 25 April 2022

In 1983, Korb, C. L. et al.,(1983) of Laboratory for Atmospheres, NASA Goddard Space Flight Center, proposed a method of detecting atmospheric pressure using differential absorption LIDAR and the trough between oxygen absorption lines. In 1987, Schwemmer et al.(1987) structured a novel differential absorption LIDAR system. It employs a flash-pump alexandrite laser to emit a beam of two wavelengths of approximately13160cm^{-1},coupled with an oxygen photoacoustic absorption cell and a high-precision wavelength meter to stabilize the emission wavelength. Moreover, the seed source is a continuous wave from either a Ti:sapphire single longitudinal mode laser or a diode laser(Schwemmer et al., 1987). In June and July 1989, a series of flight measurement tests were conducted on the east coast of the United States(Korb et al., 1989). In 1999, Flamant, C. N., Schwemmer, G. K. Korb, C. L., Evans, K. D. and Palm, S. P. published their report "Pressure measurements Using and Airborne Differential absorption LIDAR. Part I: Analysis of the systematic error sources,"(Flamant et al., 1999) where in the instrumental and systematic error sources of differential absorption LIDAR was analyzed when measuring atmospheric pressure profile.

In the ASCENDS (Active Sensing of CO_2 Emission over Nights, Days, and Seasons) program, the surface pressure was determined to accurately measure the CO_2 dry mixing ratio(Zaccheo et al., 2014; Crowell, et al., 2015). Between 2007 and 2013Stephen, M. Krainak, M. Riris, H. and others of NASA Goddard Space Flight Center and Allan, G. R. of Sigma Space Corporation reported on the use of an aircraft as a platform and transmitter to continuously send out pulse trains of multiple wavelengths of approximately 764.7nm with the receiver receiving the return echoes.(Stephen et al., 2007-2008; Riris et al., 2012-2013,2017) Thus, multiple pulse train return signals were accumulated, using which the oxygen absorption spectrum curve of the 764.5–764.9nm trough segment was plotted. Subsequently, the differential optical depth of oxygen was calculated from the transmittance curve.

Dual-wavelength (detection/reference wavelengths) laser pulses are launched downwards from the space platform(Millán et al., 2014); consequently, the reflected laser pulses energy from the earth's surface or the top of a cloud are received. Subsequently, the atmospheric optical depth and flight time of the laser pulses passing through the air column are measured. Thus, the atmospheric pressure and altitude of the surface/cloud top can be simultaneously obtained, and the top of the cloud ground can be distinguished from the ground. Such data is meaningful for various meteorological applications. By obtaining the pressure values on the surface and cloud tops and combining the results with a vertical temperature profile obtained from other sensors or weather models and utilizing statistical equations, the vertical profile of atmospheric pressure can be obtained. The differential absorption LIDAR is installed on a sun-synchronous orbit, and it makes a polar orbit around the earth from south to north. It allows much denser surface/cloud top atmospheric pressure data than ground meteorological stations to be obtained.

This paper is structured as follow. Section 1 presents the Introduction, and Section 2, the mechanism of differential absorption LIDAR for detecting surface pressure was introduced. whereas Section 3 evaluates the performance of a differential absorption LIDAR model, Finally, Section 4 presents the summary.

2 Mechanism of Differential Absorption LIDAR to Detect Atmospheric Pressure

Differential absorption LIDAR selects two wavelengths in the A absorption band of oxygen (759–770nm). The laser beam with one wavelength value passes through the atmosphere twice; its absorption coefficient, although insensitive to changes in atmospheric temperature, is sensitive to variations in atmospheric pressure. This wavelength is referred to as the detection wavelength (online).Further, the absorption coefficient of another wavelength from the laser beam passing through the atmosphere twice is relatively smaller, and it is referred to as the reference wavelength (offline), with its value being close to the detection wavelength.

https://doi.org/10.5194/amt-2022-69
Preprint. Discussion started: 25 April 2022

Let the atmospheric pressure at altitude R_0, where the LIDAR is located, be $p(R_0)$; the atmospheric pressure at altitude R be $p(R)$; and $g(z)$ be the gravitational acceleration at altitude z. The difference in the atmospheric pressure between altitude R_0 and R is equal to the weight of the air column between R_0 and R per unit area, where the dry air molecular mass m_{dry}=28.9644 g/mol and water vapor molecular mass m_{wv}=18 g/mol.

Atmospheric quasi-static equation:

$$dp = -n_{dry}(z) \cdot \left(m_{dry} + m_{wv}\chi_{wv}(z)\right) \cdot g(z)dz \tag{1}$$

Gas state equation:

$$p(z) = n_{dry}(z) \cdot (1 + \chi_{wv}(z)) \cdot kT(z) \tag{2}$$

$$p(R) = p_{surface} \cdot exp^{-\int_0^R \frac{\left(m_{dry}+m_{wv}\chi_{wv}(z)\right)g(z)}{kT(z)(1+\chi_{wv}(z))}dz} \tag{3}$$

This integration is performed at an altitude z, $n_{dry}(z)$ is the density of dry air molecules, $\chi_{wv}(z)$ is the water vapor volume mixing ratio, $p_{surface}$ is the surface pressure, and k is the Boltzmann constant. Thus, by remote sensing the weight or mass per unit area of a vertical air column between two altitudes, the difference in atmospheric pressure between these two altitudes can be obtained.

Oxygen is among the most stable components in the atmosphere in terms of space and time. $n_{O_2}(z)$ is the number density of oxygen molecules at altitude z. The number of oxygen molecules accounts for a fixed proportion of 20.948% of the number of dry air atmospheric molecules. Further, the optical depth of the atmosphere between R_0 and R is the integral of its extinction coefficient with respect to the beam path, which can be expressed as

$$OD(R_0, R) = \int_{R_0}^{R}\left[\alpha_a(v,z) + \alpha_m(v,z) + n_{O_2}(z)\sigma(v, p(z), T(z))\right]dz \tag{4}$$

where OD is the optical depth in Beer's theorem, σ is the absorption cross-section of the oxygen molecule to the A-band λ wavelength, and $\Delta\sigma$ is the difference $\sigma(\lambda_{on}, p(z), T(z))$-$\sigma(\lambda_{off}, p(z), T(z))$. Further, $\alpha_a(\lambda, z)$ and $\alpha_m(\lambda, z)$ are the aerosol extinction coefficient and the extinction coefficient of atmospheric molecules except for oxygen absorption, respectively, and $n_{O_2}(z)\sigma(\lambda, p(z), T(z))$ is the oxygen absorption coefficient of the corresponding wavelength. The difference in the single-pass optical depth compared to the dual-wavelength between R_0 and R is referred to as the differential optical depth $dOD(R_0, R)$.Although the weight of the atmospheric column between R_0 and R per unit area is unknown, the differential optical depth can be expressed as

$$dOD(R_0, R) = \int_{R_0}^{R} n_{O_2}(z)\left(\sigma(v_{on}, z) - \sigma(v_{off}, z)\right)dz \tag{5}$$

$$n_{O_2}(z) = \frac{0.20948p(z)}{kT(z)\cdot(1+\chi(z))} \tag{6}$$

where $N_{s,on}(R)/N_{s,off}(R)$ represents the online/offline dual-wavelength echo pulse energy (number of photons) received by the LIDAR, which is expressed using the LIDAR equations as follows:

$$N_{s,on}(R) = \frac{c}{2}\frac{A_r}{R^2}\frac{\rho}{\pi}E_{on}\eta_r\eta_d \times exp[-2OD(R_0, R)] \tag{7}$$

$$N_{s,off}(R) = \frac{c}{2}\frac{A_r}{R^2}\frac{\rho}{\pi}E_{off}\eta_r\eta_d \times exp[-2OD(R_0, R)] \tag{8}$$

Where E_{on}/E_{off} is the energy of a single shot emitted laser for both online/offline. Further, η_r is the receiving efficiency of light beam, η_d is the quantum efficiency of the detector, and A_r is the effective receiving area of the telescope. In the space-to-earth observation, IPDA, receives return echo from hard targets on the ground, and ρ represents the reflectivity of ground targets.

https://doi.org/10.5194/amt-2022-69
Preprint. Discussion started: 25 April 2022

The beam of dual-wavelength has the same path, receiving/sending time, footprint, and random process in the atmosphere. Further, except for $\sigma(\lambda,p(z),T(z))$, all other parameters are considered to be similar (but not equal). Dividing Eq. (7) by Eq. (8), the differential optical depth can be calculated by measuring the energy of the pulse emitted and the energy of received return echo by the LIDAR as follows:

$$dOD(R_0,R) = -\frac{1}{2} ln\left\{\left[\frac{N_{on}(R)}{N_{off}(R)}\right]\left(\frac{E_{off}}{E_{on}}\right)\right\} + C \quad (9)$$

$$C = \int_{R_0}^{R}\left[\alpha_a(v_{on},z) - \alpha_a(v_{off},z)\right] dz + \int_{R_0}^{R}\left[\alpha_m(v_{on},z) - \alpha_m(v_{off},z)\right] dz \quad (10)$$

where C represents a systematic error between the $\frac{1}{2} ln\left(\frac{N_{off}(R)}{N_{on}(R)}\frac{E_{on}}{E_{off}}\right)$ value calculated from the LIDAR data and the differential optical depth. Thus, laser shots of these two wavelengths are simultaneously emitted and the reflections from the surface/cloud tops are received. However, owing to the difference in oxygen absorption, the atmospheric transmittance of the two wavelengths is different. The logarithm of the ratio of $\frac{N_{off}(R)}{N_{on}(R)}\frac{E_{on}}{E_{off}}$ can be used to obtain the atmospheric differential optical depth from the satellite to the surface/cloud top. IPDA launches several laser pulses from the space platform to the ground, and it detects the surface pressure, with point R_0representing the satellite location. Further, there is almost no air pressure $p(R_0)$=0.0, and $p(R)$ represents the surface pressure $p_{surface}$.

In the path of the laser beam, only the section from the altitude of 71km to the ground has a significant effect on the optical depth, whereas the effect of atmosphere above 71km can be ignored. Further, the gravitational acceleration $g(z)$ can be regarded as a constant 9.80616 N/m^2at atmospheric altitude below 71 km.

On transforming the elevation z coordinates in Eq. (1) into atmospheric pressure p coordinates, the following is obtained

$$n_{dry}(z)dz = \frac{dp}{(m_{dry}+m_{wv}\chi_{wv}(p))g(p)} \quad (11)$$

Thus, the absorption cross-section $\sigma(\lambda, p(z), T(z))$ is related to atmospheric temperature and pressure, and thus it can be rewritten as $\sigma(\lambda, p, T(p))$ in pressure p coordinates. Combining Eq. (11), we can transform Eq. (5) from the elevation z coordinate to the pressure p coordinate. The differential optical depth dOD associated with pressure p coordinates is expressed by

$$dOD(p_{ground}, p_{top}) = 0.20948 \int_{p_{top}}^{p_{ground}} \frac{\Delta\sigma(v,p,T(p))}{(m_{dry}+m_{wv}\chi_{wv}(p))g(p)} dp \quad (12)$$

Here we assume that the pressure at the top of the atmosphere is p_{top}=0.0, and the atmospheric pressure at the surface (or cloud top) $p_{ground}=p_{surface}$.

$$dOD(p_{surface}) = \frac{0.20948}{g} \int_0^{p_{surface}} \frac{\sigma(v_{on},p,T(p)) - \sigma(v_{off},p,T(p))}{m_{dry}+m_{wv}\chi_{wv}(p)} dp \quad (13)$$

Equation (13) establishes the implicit expression of the differential optical depth of the entire aerosphere with respect to the surface pressure $p_{surface}$. Theoretically, the true value of the differential optical depth is the state of the atmosphere and is not related to the LIDAR parameters. Further, it is independent of the measurement method. However, the measurement error of the differential optical depth is closely related to the LIDAR parameters. In the pressure p coordinate, the differential optical depth dOD ($p_{surface}$)is expressed through the integral Eq. (14) as follows:

$$dOD(p_{surface}) = \int_0^{p_{surface}} \frac{\sigma(v_{on},p,T(p)) - \sigma(v_{off},p,T(p))}{2.251667\times10^{-24}\times(1+0.6214\chi_{wv}(p))} dp \quad (14)$$

https://doi.org/10.5194/amt-2022-69
Preprint. Discussion started: 25 April 2022

On differentiating both sides of Eq. (13) with respect to $p_{surface}$ and considering the derivative function of dOD ($p_{surface}$) with respect to $p_{surface}$, we obtain

$$\frac{\partial(dOD(p_{surface}))}{\partial p_{surface}} = \frac{1}{46.8119} \times \frac{\sigma(\nu_{on}, p_{surface}, T(p_{surface})) - \sigma(\nu_{off}, p_{surface}, T(p_{surface}))}{m_{dry} + m_{wv}\chi_{wv}(p_{surface})} \quad (15)$$

Subsequently, the relationship between the errors of the surface pressure and the differential optical depth of the entire atmosphere is obtained as

$$\delta p_{surface} = \frac{46.8199 \times [m_{dry} + m_{wv}\chi_{wv}(p_{surface})]}{\sigma(\nu_{on}, p_{surface}, T(p_{surface})) - \sigma(\nu_{off}, p_{surface}, T(p_{surface}))} \delta[dOD(p_{surface})] \quad (16)$$

Assuming that the vertical profile of atmospheric temperature $T(R)$ and the vertical profile of water vapor mixing ratio $\chi_{wv}(R)$ are known from data obtained from other sensors or weather models, the surface pressure can be inversed from the differential optical depth of the entire atmosphere. The steps are shown in Fig. 1.

a. The differential optical depth measurement value $(dOD)_m$ of the atmosphere from the echo signal N_s and emission energy E of the differential absorption LIDAR is calculated.

b. Utilizing the atmospheric temperature profile $T(R)$ coupled with the pressure profile and the surface pressure in the standard atmosphere mode as the initial value of the atmospheric pressure profile $p_1(R)$ and the initial value of the surface pressure $p_{surface,1}$, respectively, and using the oxygen HITRAN database, the initial value of the absorption coefficient profile of the entire atmosphere is calculated. Thereafter, the initial value of the differential optical depth $(dOD)_{c,1}$ of the entire atmosphere is calculated.

c. If the differential optical depth $(dOD)_{c,i}$ of the entire atmosphere is numerically calculated in i-th cycle and $(dOD)_{c,i}$ is not equal to the differential optical depth $(dOD)_m$ measured by the LIDAR, then the surface pressure $p_{surface,i}$ calculated using the numerical value is not equal to the true value $p_{surface}$ of the pressure at the footprint, and thus,$(dOD)_m$ is subtracted from$(dOD)_{c,i}$.

d. The surface pressure varies with the differential optical depth. In the i-th cycle, the difference between $(dOD)_{c,i}$ and $(dOD)_m$ is multiplied by a coefficient $\frac{46.8199 \times [m_{dry} + m_{wv}\chi_{wv}(surface,i)]}{\sigma(\nu_{on}, p_{surface,i}, T_{surface,i}) - \sigma(\nu_{off}, p_{surface,i}, T_{surface,i})}$in Eq. (16) as the compensation amount and added to the calculated value of the surface pressure $p_{surface,i}$.Consequently, the resulting sum is used as the new surface pressure $p_{surface,i+1}$; $p_{surface,i+1} = p_{surface,i} + \frac{46.8199 \times [m_{dry} + m_{wv}\chi_{wv}(surface,i)]}{\sigma(\nu_{on}, p_{surface,i}, T_{surface,i}) - \sigma(\nu_{off}, p_{surface,i}, T_{surface,i})}(dOD_{c,i} - dOD_m)$.

e. Subsequently, with atmospheric temperature profile $T(R)$ and water vapor mixing ratio $\chi_{wv}(R)$ provided by other sensors or numerical weather models, coupled with the surface pressure result $p_{surface,i}$ obtained in the i+1-th cycle, the atmospheric pressure profile p_{i+1}(R) is calculated,$p_{i+1}(R) = p_{surface,i} \cdot exp^{-\int_0^R \frac{(m_{dry} + m_{wv}\chi_{wv}(z))g(z)}{kT(z)(1+\chi_{wv}(z))}dz}$.

f. Further, with the atmospheric temperature profile $T(R)$, profile for water vapor mixing ratio $\chi_{wv}(R)$, and the atmospheric pressure profile $p_{i+1}(R)$, based on the HITRAN database, differential optical depth $(dOD)_{c,i+1}$calculations are repeated.

g. Repeat steps c–f. In the case of the above iterative process, with increase in i, the difference between $(dOD)_{c,i}$ and $(dOD)_m$ decreases till $i=M$, $p_{surface,\ M+1}$ - $p_{surface,M}$ is comparable to the error. If that happens, the iterative loop stops. Herein, the output surface pressure $p_{surface,M}$ calculation result is considered to be sufficiently close to the true value $p_{surface}$.

https://doi.org/10.5194/amt-2022-69
Preprint. Discussion started: 25 April 2022

Atmospheric Measurement Techniques
Discussions

The above calculation steps also suggest that the parameters related to the temperature, pressure, and humidity of the atmosphere should be detected synchronously in the future, as input conditions for each other, and simultaneously iterated.

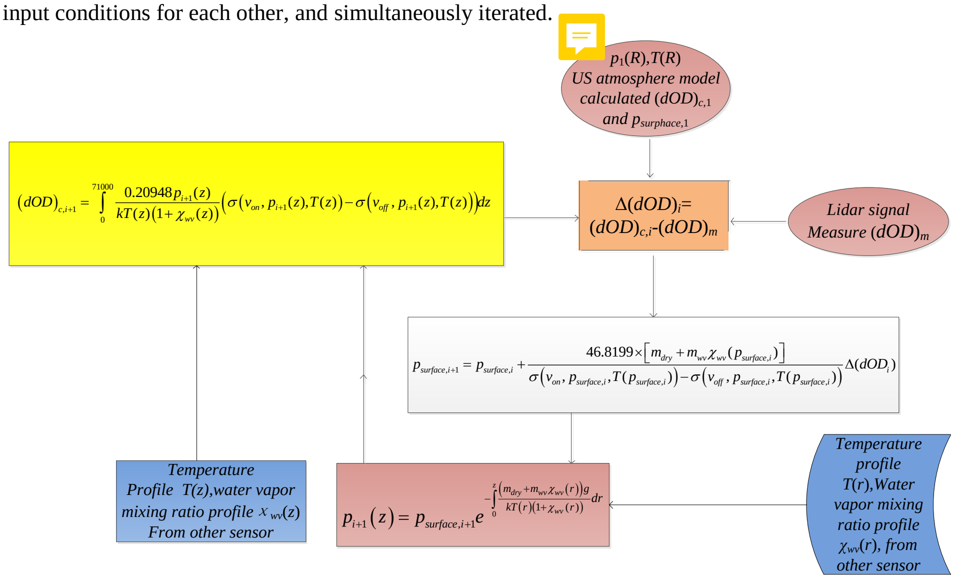

Figure 1: Iterative calculation process of the atmospheric pressure on the surface of the differential optical depth measured by the differential absorption LIDAR.

3 Performance evaluation of an integrated path differential absorption LIDAR model

3.1 A-band absorption spectrum of Oxygen

The absorption line of oxygen molecules is broadened in the atmosphere via collision and Doppler broadening. They are expressed via the famous Lorentz and Gauss line shapes, respectively. Below 15km in the atmosphere, collision broadening is dominant, with "*n*" representing the sensitivity factor of collision broadening with respect to air temperature, that is, the average value of its own broadening and nitrogen broadening sensitivity factors. We consider n=0.73–0.59 from HITRAN database, normal pressure p_0=1013.25hPa, normal temperature T_0=296K, γ_0 is the pressure broadening under normal temperature and normal pressure, S_0 is the intensity of the absorption line at room temperature and pressure, σ_0 is the peak absorption cross section of the absorption line at room temperature and pressure, c is the speed of light, h is the Planck constant, m is the molecular mass of oxygen, and v_0(cm^{-1}) represents the position of the center wave number (light frequency) of the absorption line. Further, E'' is the energy of the low-energy state of the electron. Moreover, in the application of differential absorption LIDAR, the absorption line shape of the oxygen molecule can be represented using the Voigt line shape, which is a form of the convolution Gauss line shape with Lorentz line shape. The arbitrary real number t is the variable of the Voigt linear integral. The absorption cross-section $\sigma(v)$ at the light wave number v is written as $\sigma(v) = \sigma_0 \frac{y}{\pi}\int_{-\infty}^{\infty}\frac{exp(-t^2)}{y^2+(x-t)^2}dt$, where $x = \left(\frac{v-v_0}{v_0}\right)\left(\frac{m}{2kT}\right)^{0.5} c$ and $y = v_0\gamma_0\left(\frac{p}{p_0}\right)\left(\frac{T_0}{T}\right)^n\left(\frac{m}{2kT}\right)^{0.5} c$, and $\sigma_0 = \frac{S_0 c}{v_0}\left(\frac{2\pi kT}{m}\right)^{0.5}\left(\frac{T_0}{T}\right)^{1.5} exp\left[\frac{E''c}{k}\left(\frac{1}{T_0}-\frac{1}{T}\right)\right]$.The wavelength in the trough between the oxygen absorption line P13Q12 and P13P13, between the oxygen absorption line P15P15 and P15Q14, and even absorption lines P17Q16 and P17P17 can be selected as the detection

https://doi.org/10.5194/amt-2022-69
Preprint. Discussion started: 25 April 2022

Atmospheric Measurement Techniques Discussions

wavelength. Table 1 lists certain parameters of the six absorption lines: for example, the linear function $\sigma_q(v\text{-}v_{01})$ of the absorption cross-section of the oxygen absorption line P13Q12 with respect to the wave number v, and the line function $\sigma_p(v\text{-}v_{02})$ of the absorption cross section of the P13P13 with respect to the wave number v. Further, the wavelength λ_{on} (wavenumber v_{on}) we selected is located at the minimum of the absorption cross-section between the two spectral lines, that is, its absorption cross-section is the superposition of the values of the extension lines of two adjacent Voigt linear functions at v_{on}. Moreover, its absorption cross-section $\sigma_{on}(v)= \sigma_p(v_{on})+\sigma_q(v_{on})$—the wings of the two Voigt lineshape functions—is the manifestation of their pressure expansion.

Table 1 Parameters of the three groups of absorption lines of Oxygen A(296K) (Brown and Plymate, 2014)

Assignment	Line center	Intensity	Low energy	Half Widths γ_0		Pressure-introduced shift	Temperature dependence
	v_0	S_0	E''	γ_{air}	γ_{self}	Average(δ)	n
	cm^{-1}	cm mole^{-1}	cm^{-1}	cm^{-1}/atm	cm^{-1}/atm	cm^{-1}/atm	
P13Q12	13078.2275	5.61×10^{-24}	260.6824	0.0466 (0.6)	0.0461 (1.1)	-0.0061	0.73
P13P13	13076.3273	6.13×10^{-24}	262.5827	0.0467 (0.8)	0.0460 (1.1)	-0.0068	0.73
P15Q14	13069.9619	4.33×10^{-24}	343.9694	0.0457 (1.2)	0.0449 (1.6)	-0.0051	0.73
P15P15	13068.0818	4.68×10^{-24}	345.8495	0.0455 (1.2)	0.0452 (1.6)	-0.0064	0.73
P17Q16	13061.3273	3.09×10^{-24}	438.7010	0.044	0.045	-0.00898	0.73
P17P17	13059.4665	3.31×10^{-24}	440.5618	0.0452	0.045	-0.00902	0.59

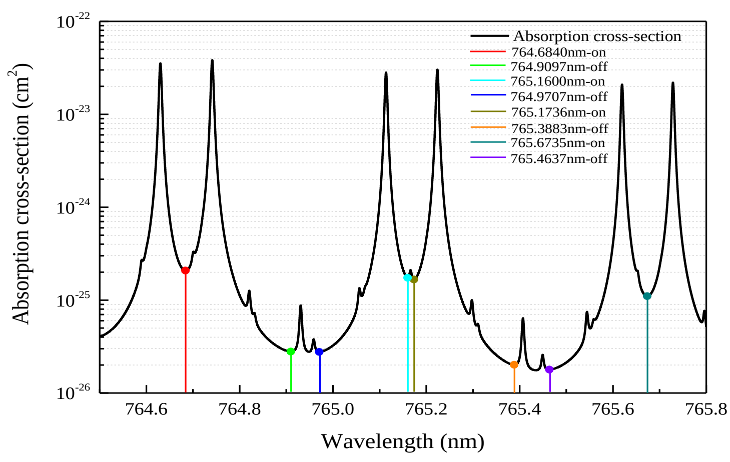

(a)

https://doi.org/10.5194/amt-2022-69
Preprint. Discussion started: 25 April 2022

Atmospheric Measurement Techniques
Open Access
Discussions

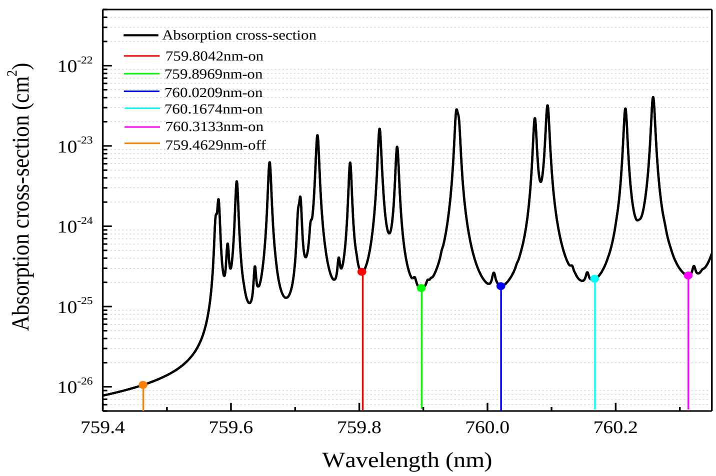

(b)

Figure 2: (a)Near-ground absorption cross-section near 765nm,(b)Near-ground absorption cross-section near 760nm

Within the A absorption band of oxygen (759–770nm), the spectral transmittances in the vicinity of 760 and 765nm were relatively insensitive to temperature, this band is the low interference of water vapor and carbon dioxide molecules. Further,the atmospheric transmittance at 760nm is lower than the atmospheric transmittance at 765nm, and when ground-based LIDAR (RR-DIAL) detects tropospheric backscattering owing to the round-trip optical path being shorter, two adjacent lines near 760nm can be selected. In addition, the plots of absorption spectra shown in Figure 2, the Oxygen absorption features with a number of smaller and sharper absorption spikes, it contains isotopologues of Oxygen molecules, showing some subtle differences, the wavelength in the middle of the trough area between lines is more suitable as the ~~detection wavelength~~ online and the reference ~~wavelength offline~~ (Korb et al., 1983,1989; Schwemmer, et al., 1987). When IPDA ~~shoots lasers~~ from the satellite and receives the echo from the ground surface, the laser beam that passes through the entire atmosphere twice results in the path being longer. Thus, 765nm is relatively more suitable for remote sensing of surface pressure from satellites(Riris et al., 2017).

https://doi.org/10.5194/amt-2022-69
Preprint. Discussion started: 25 April 2022

Atmospheric Measurement Techniques Discussions

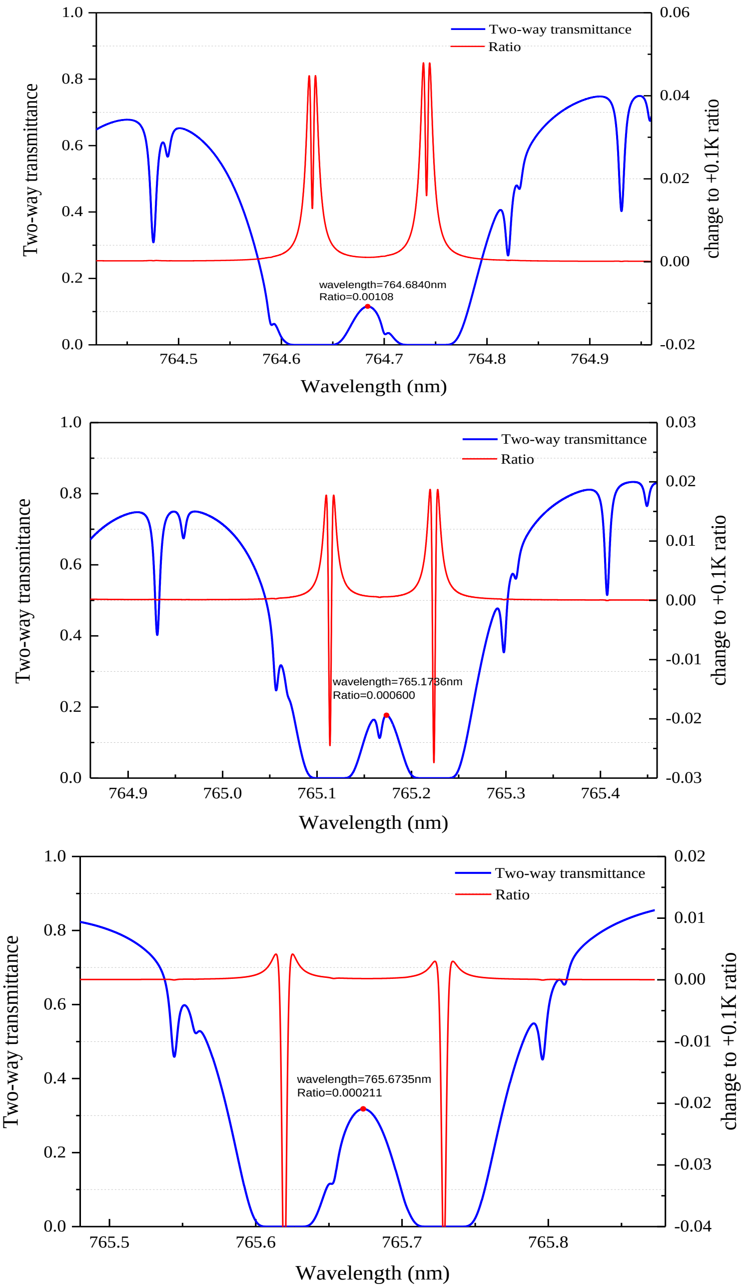

Figure 3: Transmittance spectra of three intervals around 765nm and their ratio to 0.1K change in temperature

https://doi.org/10.5194/amt-2022-69
Preprint. Discussion started: 25 April 2022

Atmospheric Measurement Techniques Discussions

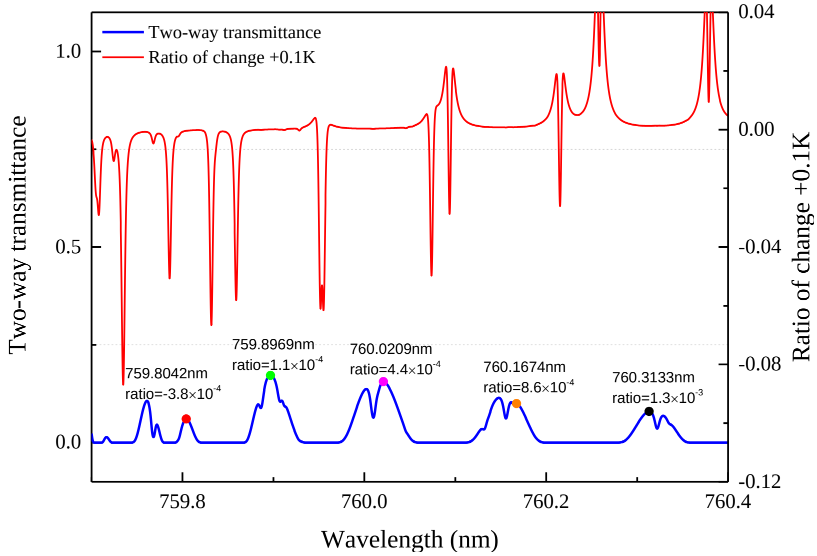

Figure 4: Transmittance spectra around 760nm and their ratio to 0.1K change in temperature

The absorptive optical depth of oxygen $dOD(p_{surface})$ with respect to the path 0–71km corresponds to the optical transmittance e^{-2dOD} of this path with respect to the *v* wavenumber. Figure 3 shows the transmittance spectra of three intervals around 765nm and their sensitivity to temperature changes of +0.1K.Similarly, Figure 4 shows the transmittance spectra of around 760nm and their sensitivity to temperature changes of +0.1K.

Table 2 differential optical depth and differential absorption cross section of 9 pairs of wavelengths in standard atmospheric mode

Wavelength(nm)		$\int_0^{71}(\alpha_m+\alpha_a)dz$	$\int_0^{71}(n_{O_2}\sigma)dz$	OD(0,71km)	σ_{O_2} (cm^2)	dOD(0,71km)	$\Delta\sigma_{O_2}$ (cm^2)
on	764.6840	0.1852	0.493	0.678	2.08×10^{-25}	0.428	1.80×10^{-25}
off	764.9097	0.1851	0.0653	0.251	2.80×10^{-26}		
on	765.1600	0.1851	0.389	0.574	1.74×10^{-25}	0.325	1.46×10^{-25}
off	764.9707	0.1851	0.0638	0.249	2.77×10^{-26}		
on	765.1736	0.1849	0.373	0.558	1.67×10^{-25}	0.328	1.47×10^{-25}
off	765.3883	0.1849	0.0448	0.230	2.01×10^{-26}		

https://doi.org/10.5194/amt-2022-69
Preprint. Discussion started: 25 April 2022

on	765.6735	0.1848	0.231	0.416	1.10×10^{-25}	0.192	9.25×10^{-26}
off	765.4637	0.1849	0.0391	0.224	1.78×10^{-26}		
on	759.8042	0.1872	0.515	0.702	2.60×10^{-25}	0.493	2.49×10^{-25}
off	759.4629	0.1873	0.0216	0.209	1.46×10^{-26}		
on	759.8969	0.1871	0.343	0.530	1.66×10^{-25}	0.321	1.55×10^{-25}
off	759.4629	0.1873	0.0216	0.209	1.46×10^{-26}		
on	760.0209	0.1871	0.385	0.573	1.77×10^{-25}	0.364	1.67×10^{-25}
off	759.4629	0.1873	0.0216	0.209	1.46×10^{-26}		
on	760.1674	0.1870	0.506	0.693	2.22×10^{-25}	0.484	2.12×10^{-25}
off	759.4629	0.1873	0.0216	0.209	1.46×10^{-26}		
on	760.3133	0.1870	0.576	0.763	2.46×10^{-25}	0.554	2.36×10^{-25}
off	759.4629	0.1873	0.0216	0.209	1.46×10^{-26}		

Equation (16) clearly indicates that in various factors that result in $\delta[dOD(p_{\mathrm{surface}})]$, the error of differential optical depth conditionally causes conditionally causes the error $\delta p_{surface}$ of the surface pressure. Additionally, the detection wavelength absorption cross-section difference $\Delta\sigma(p_{surface})$ near the ground is inversely proportional to the surface pressure error. Evidently, a key factor affecting DIAL sensitivity is the online and offline wavelength positions. However, for the candidate wavelengths marked in Fig. 2 used as detection wavelengths, each would offer its own advantages and disadvantages, and consequently, comprehensive evaluation is required.

3.2 Differential absorption LIDAR system model

The research results reported by Coney, *et al.*(Munk et al., 2016-2019; Coney et al., 2021; Thomas et al., 2016; Strotkamp et al., 2019)along with those reported by Wulfmeyer and ̇osenberg et al.(1996), refer to the ADM-Aeolus in orbit ALADIN system parameters of the Aeolus mission (Lemmerz et al., 2017); the receiver is based on the GLAS-Mission-1064nm receiver, the orbit altitude is 400km, and diameter of the telescope is 1.5m. Consequently, the model parameters of the differential absorption LIDAR has been proposed, as shown in Table 3. The transmitter model parameters, with the exception of the pulse energy of 100mJ, have been separately reported in different documents(Coney et al., 2021).However, these indicators have been achieved in the same laser, and thus, more research is required.

Table 3 System parameters of differential absorption LIDAR

Transmitter	
Laser pulse energy	100mJ

https://doi.org/10.5194/amt-2022-69
Preprint. Discussion started: 25 April 2022

Laser pulse Width	88ns
Pulse repetition rate	100Hz
Laser Divergence Angle	90μrad for±3σ
Spectral purity	99.99%
Pointing stability	< 10μrad
Receiver	
Telescope Diameter (A_r)	1.5m(SiC)
Receiver Field-of-view (full)	100μrad
Optical Filter Bandwidth (*FW*)	0.8nm(FWHM)
Fabry-Perot Elton (thickness=2mm)	25pm(free spectral range ≈ 0.1nm)
Receiver Efficiency	50%
Combined filter width	0.025nm
Detector and amplifier	
Detector(Laser Components DG, Inc)	Si-APD(SAR1500/C30956/S3884-04)
APD Quantum Efficiency (η_d)	75%
Detector Diameter	Φ1.5mm
Electronic system bandwidth (*BW*)	3MHz
APD dark current (I_d)	1nA type
APD gain(*M*)	100
APD excess noise factor(*F*)	2.4
APD capacitance (C_d)	4pF
trans-impedance amplifier gain (R_f)	20kV/A
trans-impedance amplifier input current noise (I_{nA})	2.5pA/Hz$^{1/2}$
trans-impedance amplifier input voltage noise (V_{nA})	20nV/Hz$^{1/2}$
operate temperature	293 K
Platform and environment	
Orbit altitude and velocity	400 km, 7 km/s
Orbit type	Polar, sun synchronous, dawn/dusk
Along-track resolution	44 km
Simulation top altitude	71 km
Viewing geometry	Nadir
Atmosphere model	US standard atmosphere
Aerosol model	Median aerosol profile
(765nm)the surface albedo over ocean/land	0.1575/0.314
Pointing stability	< 50μrad
Spectroscopic data base	HITRAN 2012

As reported in reference (Lancaster et al., 2005), the equivalent Lambertian reflection coefficient of the sub-satellite point laser on the ocean surface has an empirical relationship $\rho_{eff} = \frac{\rho}{4\langle S^2\rangle}$,where the Fresnel reflection coefficient is ρ = 0.02, and $<S^2>$ is the variance of the wave steepness distribution. Further, Bufton et al.(1983)and Menzies et al.(1998)individually adopted relationship as follows:

https://doi.org/10.5194/amt-2022-69
Preprint. Discussion started: 25 April 2022

Atmospheric Measurement Techniques Discussions

$$\langle S^2 \rangle = \begin{cases} (\ln U_{10} + 1.2) \times 10^{-2} & U_{10} \le 7.0m/s \\ (0.85 \ln U_{10} - 1.45) \times 10^{-1} & U_{10} > 7.0m/s \end{cases} \quad (17)$$

where U_{10} is the wind speed of segment 10m above the ocean surface. The general ocean surface wind speed is taken as 8m/s, whereas ρ_{eff} = 0.1575 and ρ_{eff}/π = 0.025sr^{-1}. In addition, the reflectivity of terrestrial lasers is generally 0.314.

3.3 Performance evaluation of A-band DIAL system

3.3.1 Random error of differential optical depth caused by noise

The number of received return echo photons $N_{s,on}$ and $N_{s,off}$ is obtained using the LIDAR Eq. (7) and Eq.(8). Equations(18)–(25) are commonly used for the on and off channels.

$$N_s(R_0, R) = \frac{\lambda \cdot E}{h \cdot c} \cdot A_r \cdot \eta_d \cdot \eta_r \cdot \left(\frac{\rho}{\pi}\right) . \frac{exp[-2OD(R_0,R)]}{(R_0 - R)^2} \quad (18)$$

Here the working and reference wavelengths λ_{on} and λ_{off}, the Planck constant is h, ρ is the surface reflectivity, and c is the speed of light. Further, the effective pulse width τ_w of the echo signal is a combination of the emitted laser pulse width τ_L, and the detection electronic system bandwidth BW (unit Hz), effective target altitude within the laser footprint ΔH, R-R_0=400km,ΔH=2 m, can be expressed as (Ehret, et al., 2008):

$$\tau_w = \sqrt{\tau_L^2 + \left(\frac{1}{3} \cdot BW\right)^2 + \left(\frac{2 \cdot \Delta H}{c}\right)^2} \quad (19)$$

The background signal N_{BG} (photoelectrons), assuming a Lambertian surface and zenith sun, is calculated as

$$N_{BG}(\lambda) = \frac{\lambda \cdot S_{BG}}{h \cdot c} \tau_w \cdot A_r \cdot \eta_d \cdot \eta_r \cdot \left(\frac{\rho}{\pi}\right) \cdot \left(\frac{FOV}{2}\right)^2 \pi \cdot FW . exp[-2OD(R_0, R)] \quad (20)$$

where S_{BG} is the exo-atmospheric solar irradiance value (1.221W m^{-2} nm^{-1})(ASTM international, United States, 2019)at 765nm, FW is the bandwidth of the optical filter (0.025nm×4) and the field of view (FOV) (unit rad) of the FOV receiving telescope. The bandwidth of the Fabry–Perot etalon, free spectral range, and width of the narrowband filler were 25pm,0.1nm, and 0.8nm, respectively. There are 8 longitudinal modes of Fabry–Perot etalon that can pass through. However, the transmittance of each longitudinal mode is different, and thus, the equivalent solar window width is 25pm×4 = 0.1nm. Further, the backscattering coefficient (ρ/π) on the surface of land such as ocean and vegetation during the daytime (Thomas et al., 2016), and ρ were calculated as 0.1575 and 0.314, respectively.

Here the q electrons charge is 1.6×10^{-19} C, M is the gain of silicon avalanche diode (APD). The total noise associated with the detection signal is divided into fixed circuit noise and signal-dependent shot noise. The total circuit noise current spectral density (unit A/Hz$^{1/2}$) I_n, can be expressed as (Refaat, et al., 2013)

$$I_n = \sqrt{2 \cdot q \cdot I_d \cdot M \cdot F + I_{nA}^2 + \frac{V_{nA}^2}{R_f^2} + \frac{4 \cdot k \cdot T}{R_f + \frac{(2 \cdot \pi \cdot V_{nA} \cdot C_d \cdot BW)^2}{3}}} \quad (21)$$

where I_d and F are the dark current and excess noise factors of the detector, respectively; I_{nA} and V_{nA} are the preamplifier integrated input current and input voltage noise spectral density, respectively; R_f is the feedback resistance of the preamplifier; and C_d is the equivalent input capacitance of the amplifier and the detector. The circuit noise is often limited by the shot noise of the dark current of the detector or the noise of the preamplifier. In this analysis, all circuit noises refer to the detector input and the equivalent circuit noise-generated photoelectrons, and $N_{n,C}$, is calculated as

https://doi.org/10.5194/amt-2022-69
Preprint. Discussion started: 25 April 2022

$$N_{n,C} = \frac{I_n \cdot \tau_w \cdot \sqrt{BW}}{q \cdot M} \quad (22)$$

Similarly, the equivalent shot noise-generated photoelectrons, $N_{n,S,}$ are calculated as

$$N_{n,S} = \sqrt{2 \cdot N_S \cdot F \cdot \tau_w \cdot BW} \quad (23)$$

Further, the photoelectron $N_{n,BG}$, equivalent to the equivalent shot noise associated with the background radiation can be calculated as

$$N_{n,BG} = \sqrt{2 \cdot N_{BG} \cdot F \cdot \tau_w \cdot BW} \quad (24)$$

These noises are regarded as the equivalent photoelectron number generated in the detector (before the multiplication process), and are proportional to the actual detected photoelectron number. The total signal-to-noise ratio is expressed as follows(Ehret, *et al*., 2008):

$$SNR_{on/off} = \frac{N_{s,on/off}}{\sqrt{N_{n,C}^2 + N_{n,S,on/off}^2 + N_{n,BG,on/off}^2}} \quad (25)$$

Where s is the number of echo signal pulses accumulated and averaged by the LIDAR. The error ε_R caused by the noise of the LIDAR receiving a single echo is a random error. Moreover, it is necessary to calibrate the LIDAR echo signal detection channel and the laser emission pulse energy monitoring channel to remove nonlinear and nonzero biased background voltage. Further, the calibration error and AD conversion error comprise the systematic error. In addition, the error ε_A caused by the uncertainty of atmospheric environment (atmospheric temperature profile, atmospheric water vapor mixing ratio profile), and the associated error ε_T of the laser emission characteristics (jitter of the center wavelength of the emitted beam, the emission spectrum width, and the purity of the emission spectrum) are all systematic errors. The total error of the differential optical depth can be expressed as

$$\delta[dOD] = \frac{\varepsilon_R}{\sqrt{s}} + \sqrt{{\varepsilon_A}^2 + {\varepsilon_T}^2} \quad (26)$$

Equation(9) indicates that the random noise of the echo signals $N_{on}(R)$ and $N_{off}(R)$ and the random measurement error of the pulse energies E_{on} and E_{off} result in the random error of the differential optical depth $\varepsilon_R = \delta[dOD(p_{surface})]_R$ as follows:

$$\varepsilon_R = \delta\left[dOD(p_{surface})\right]_R = \frac{1}{2}\sqrt{\left(\frac{\delta N_{s,on}(R)}{N_{s,on}(R)}\right)^2 + \left(\frac{\delta N_{s,off}(R)}{N_{s,off}(R)}\right)^2 + \left(\frac{\Delta E_{on}}{E_{on}}\right)^2 + \left(\frac{\Delta E_{off}}{E_{off}}\right)^2} \quad (27)$$

The signal-to-noise ratio of LIDAR can be calculated using Eq.(18)–(25). Simultaneously, it is considered that the measurement error of pulse energy $\Delta E_{on}/E_{on} \approx \Delta E_{off}/E_{off}$ is very small and can thus be ignored. The random error of LIDAR echo (noise) measurement is calculated as

$$\varepsilon_R = \frac{1}{2}\sqrt{SNR_{on}^{-2} + SNR_{off}^{-2}} \quad (28)$$

When the laser irradiates the ocean surface (for example, the average wind speed is 8m/s), 0.1575 represents median for the ocean surface reflectivity(Ehret, et al., 2008), and the random error ε_R of the differential optical depth is calculated considering the single pulse echo; with a time resolution of at least 6.25 s ,the distance resolution along the track of 44km and S = 625 laser pulse echoes are taken as a group for cumulative average, the random error of the atmospheric differential optical depth above the ocean surface is $\frac{\varepsilon_R}{\sqrt{625}}$.

The ocean surface possesses low laser reflectivity and weak echoes. The averaging method employed is as follows: first add up 625 echoes; thereafter subtract B and normalize,

https://doi.org/10.5194/amt-2022-69
Preprint. Discussion started: 25 April 2022

where B is the level background baseline of the LIDAR output; and finally Eq. (25) provides the differential optical depth.

$$E_{on} = \sum_{i=1}^{625} E_{i,on} \qquad (29\text{-}1)$$

$$E_{off} = \sum_{i=1}^{625} E_{i,off} \qquad (29\text{-}2)$$

$$N_{s,on} = \sum_{i=1}^{625} N_{i,s,on} \qquad (29\text{-}3)$$

$$N_{s,off} = \sum_{i=1}^{625} N_{i,s,off} \qquad (29\text{-}4)$$

$$dOD = OD_{on} - OD_{off} = -\frac{1}{2} ln\left(\frac{N_{s,on}-B}{E_{on}}\right) + \frac{1}{2} ln\left(\frac{N_{s,off}-B}{E_{off}}\right) \qquad (30)$$

Table 4 Error from noise

Wavelength(nm)	*SNR*		*Single shot Noise Error*		*average Noise Error*	
	ocean	land	ocean	land	Ocean/25	Land/12
	0.1575	0.314	0.1575	0.314	0.1575	0.314
764.6840	97.74	139.68	0.0061	0.0043	2.44×10^{-4}	3.55×10^{-4}
764.9097	152.1	215.8				
765.1600	109.0	155.5	0.0056	0.0040	2.24×10^{-4}	3.30×10^{-4}
764.9707	152.3	216.2				
765.1736	110.9	158.0	0.0055	0.0039	2.20×10^{-4}	3.24×10^{-4}
765.3883	155.4	220.5				
765.6735	128.4	182.6	0.0050	0.0035	2.00×10^{-4}	2.96×10^{-4}
765.4637	156.3	221.8				
759.8042	95.06	135.9	0.00614	0.00430	2.46×10^{-4}	3.58×10^{-4}
759.4629	158.1	224.3				
759.8969	113.7	161.9	0.00542	0.00381	2.17×10^{-4}	3.17×10^{-4}
759.4629	158.1	224.3				
760.0209	108.8	155.1	0.00558	0.00392	2.23×10^{-4}	3.27×10^{-4}
759.4629	158.1	224.3				
760.1674	95.98	137.2	0.00609	0.00427	2.44×10^{-4}	3.56×10^{-4}
759.4629	158.1	224.3				

https://doi.org/10.5194/amt-2022-69
Preprint. Discussion started: 25 April 2022

760.3133	89.15	127.7	0.00644	0.00451	2.58×10^{-4}	3.76×10^{-4}
759.4629	158.1	224.3				

It is believed that the reflectance value of 0.314 is typical and representative of the surface reflectance for most features on land (vegetation, sand, and soil). When the laser irradiates the land, the noise of the single pulse echo causes a random error in the optical depth. The time resolution of 6.25 s and resolution along track of 44 km are maintained. First, the very high footprint is highlighted, and the very low footprint points is removed. Subsequently, the average altitude of most of the remaining footprints is calculated. Considering this average altitude, all the echo pulses whose footprint altitude and the average altitude are within 2 m as a group are acquired, and the number of pulses obtained is no less than 144 pulses. Further, they are accumulated and averaged to decrease the random measurement error of the differential optical depth.

The averaging method involves first subtracting the background baseline B_i of a single echo, normalizing, and thereafter performing the cumulative average, where

$$s \geq 144, \quad \frac{N_{s,on/off}}{E_{on/off}} \approx \sum_{i=1}^{M} \frac{N_{i,s,on/off} - B_i}{E_{i,on/off}} \quad (31)$$

$$dOD = OD_{on} - OD_{off} = -\frac{1}{2} ln\left(\frac{N_{s,on}}{E_{on}}\right) + \frac{1}{2} ln\left(\frac{N_{s,off}}{E_{off}}\right) \quad (32)$$

When the laser irradiates the plain area, it is easy to confidently pick out the footprint altitude of more than 144 shots from 625 pulses. However, if uneven terrain is encountered, there are less than 144 echo pulses, difference between the footprint altitude and the average altitude is within 2 m, and average of multiple laser pulse echoes becomes unreasonable. Moreover, if greater than 144 pulses with similar footprints are still not found, this set of data is discarded.

In conclusion, when laser irradiates the ocean surface, its single echo signal is relatively weak, whereas its footprint altitude is relatively consistent; thus, more pulse echoes can be accumulated and averaged. Further, when the laser irradiates the land surface, the altitude consistency of the landing footprint is poor and accumulated average echo pulse is less, although the signal-to-noise ratio of the land single echo is relatively high.

3.3.2 Uncertainty of vertical distribution profile of atmospheric temperature

Within a certain time resolution (distance resolution), the uncertainty of the vertical profile of the atmospheric temperature results in an absolute systematic error with respect to the differential optical depth (Refaat, et al., 2013).

When the temperature change ±1K, Oxygen number density is

$$n_{O_2}(T \pm 1K) = \frac{0.20948p(z)}{k(T(z)\pm 1)\cdot(1+\chi(z))} \quad (33)$$

$$\Delta[dOD(0, surface)]_{\pm 1K} = \int_0^{71} n_{O_2}(T \pm 1K)\Delta\sigma(p(z), T(z) \pm 1)dz$$

$$- \int_0^{71} n_{O_2}(T)\Delta\sigma\big(p(z), T(z)\big)dz \quad (34)$$

Table 5 Temperature sensitivity of differential optical depth in case of ±1K uncertainty

Regimentation	$\Delta\lvert dOD(p, T-1)\rvert$	$\Delta\lvert dOD(p, T+1)\rvert$	$Max\{\Delta\lvert dC$ $-1)\rvert, \Delta\lvert d$ $-+1)\rvert\}$

https://doi.org/10.5194/amt-2022-69
Preprint. Discussion started: 25 April 2022

Atmospheric Measurement Techniques Discussions
Open Access
EGU

764.6840/ 764.9097	0.00216	0.00215	0.00216
765.1600/ 764.9707	0.000929	0.000933	0.000933
765.1736/ 765.3883	0.00102	0.00102	0.00102
765.6735/ 765.4637	0.000139	0.000146	0.000146
759.8042/ 759.4629	0.00141	0.00139	0.00141
759.8969/ 759.4629	0.000173	0.000162	0.000173
760.0209/ 759.4629	0.000624	0.000631	0.000631
760.1674/ 759.4629	0.00170	0.00170	0.00170
760.3133/ 759.4629	0.00285	0.00284	0.00285

3.3.3 Error of differential optical depth [$dOD(0, p_{surface})]_{wv}$ caused uncertainty of the mixture ratio of water vapor

The mixture ratio of near-ground water vapor in standard atmospheric mode is 1.247% higher than $\chi_{wv}(p_{surface})$.

The 20% uncertainty of profile for water vapor mixture ratio introduces uncertainty in differential optical depth $[dOD(0,p_{surface})]_{wv}$.

$$\Delta\left[dOD\left(P_{surface}\right)\right]_{\pm 20\% wv} \approx 0.20948 \int_0^{71km} \frac{p(z)}{kT(z)(1+(1\pm 20\%)\chi(z)))}\left(\sigma(\lambda_{on},z)-\sigma\left(\lambda_{off},z\right)\right)dz$$

$$-\ 0.20948 \int_0^{71km} \frac{p(z)}{kT(z)(1+\chi(z))}\left(\sigma(\lambda_{on},z)-\sigma\left(\lambda_{off},z\right)\right)dz \qquad (35)$$

Table 6 Error differential optical depth [$dOD(0, p_{surface})]_{wv}$ caused uncertainty of the mixture of water vapor

Wavelength(nm)	Differential optical depth error(20%)
764.6840 764.9097	5.29×10^{-4}
765.1600 764.9707	4.15×10^{-4}
765.1736 765.3883	4.18×10^{-4}

765.6735	2.53×10^{-4}
765.4637	
759.8042	6.71×10^{-4}
759.4629	
759.8969	4.27×10^{-4}
759.4629	
760.0209	4.71×10^{-4}
759.4629	
760.1674	6.11×10^{-4}
759.4629	
760.3133	6.88×10^{-4}
759.4629	

3.3.4 Error of the differential optical depth caused the difference in the altitude of the inner surface and between the land footprints.

The largest oxygen density is near the ground, and thus, differential optical depth is sensitive to high uncertainty near ground; ΔH=2m.

$$\Delta\left[dOD\left(P_{surface}\right)\right]_{\Delta H} \approx \int_0^{71000} n_{O_2}(z)\left(\sigma(\lambda_{on},z)-\sigma(\lambda_{off},z)\right)dz - \int_{\pm 2}^{71000} n_{O_2}(z)\left(\sigma(\lambda_{on},z)-\sigma(\lambda_{off},z)\right)dz$$

$$\approx \int_0^{\pm 2} n_{O_2}(z)\left(\sigma(\lambda_{on},z)-\sigma(\lambda_{off},z)\right)dz \quad (36)$$

Table 7 Differential optical depth error caused by the 2 m altitude difference

Wavelength	Error [*dOD*]
764.6840	0.4578×10^{-4}
764.9097	
765.1600	0.3723×10^{-4}
764.9707	
765.1736	0.3737×10^{-4}
765.3883	
765.6735	0.2356×10^{-4}
765.4637	
759.8042	0.139×10^{-4}
759.4629	
759.8969	0.0905×10^{-4}
759.4629	
760.0209	0.102×10^{-4}
759.4629	

https://doi.org/10.5194/amt-2022-69
Preprint. Discussion started: 25 April 2022

760.1674 / 759.4629	0.136×10^{-4}
760.3133 / 759.4629	0.156×10^{-4}

3.3.5 Relative error in calibration for the echo and energy monitoring channels.

The absolute error in the differential optical depth is $dOD\times 0.025\%$ (Ehret, et al., 2008), which also belongs to the systematic error.

Table 8 Calibration error for echo detection channels and energy monitoring channels

Wavelength(nm)	*dOD*(0, 71km)	error of *dOD*
764.6840 / 764.9097	0.428	1.07×10^{-4}
765.1600 / 764.9707	0.325	0.81×10^{-4}
765.1736 / 765.3883	0.328	0.82×10^{-4}
765.6735 / 765.4637	0.192	0.48×10^{-4}
759.8042 / 759.4629	0.493	1.23×10^{-4}
759.8969 / 759.4629	0.321	0.803×10^{-4}
760.0209 / 759.4629	0.364	0.910×10^{-4}
760.1674 / 759.4629	0.484	1.21×10^{-4}
760.3133 / 759.4629	0.554	1.39×10^{-4}

3.3.6 Error in optical depth due to the wavelength dependence of aerosol scattering

In the standard atmosphere mode, Mie and Rayleigh scatterings of the 765nm or 760nm dual-wavelength are similar but not equal. The coefficient C in Eq. (10) expresses the systematic error caused by the difference as follows:

$$C=\int_0^{71\mathrm{km}}[\alpha_a(\lambda_{on},z)+\alpha_m(\lambda_{on},z)]\,dz-\int_0^{71\mathrm{km}}[\alpha_a(\lambda_{off},z+\alpha_m(\lambda_{off}),z)]\,dz \qquad (37)$$

Table 9 Optical depth error caused by the wavelength dependence of the aerosol scattering

https://doi.org/10.5194/amt-2022-69
Preprint. Discussion started: 25 April 2022

Atmospheric Measurement Techniques
Discussions
Open Access
EGU

Wavelength(nm)		*C*
on	764.6840	0.90×10^{-4}
off	764.9097	
on	765.1600	0.76×10^{-4}
off	764.9707	
on	765.1736	0.86×10^{-4}
off	765.3883	
on	765.6735	0.84×10^{-4}
off	765.4637	
on	759.8042	1.39×10^{-4}
off	759.4629	
on	759.8969	1.77×10^{-4}
off	759.4629	
on	760.0209	2.28×10^{-4}
off	759.4629	
on	760.1674	2.88×10^{-4}
off	759.4629	
on	760.3133	3.47×10^{-4}
off	759.4629	

The errors in aerosol Mie scattering with the wavelength dependence error, spectral width error, and spectral purity error, can be eliminated by correction. Wavelength dependence of extinction coefficient of aerosol, 0.0<k< 2.0, k is uncertain and varies with the particle size, shape and concentration of aerosol, so it will bring systematic error of differential optical depth.

3.3.7 Error in differential optical depth from the spectral purity of the on/off laser

The spectral purity ξ of the spaceborne IPDA LIDAR is 99.99% (Wulfmeyer and ösenberg et al.1996), which results in an increase in the on-channel echo and the absolute error of the optical depth. For a spectral purity of 100%, the relationship between the two on/off channel signals is considered to be $N_{s,on}{}' = N_{s,off}{}' e^{-2dOD}$ and $dOD = -\frac{1}{2} ln\left(\frac{N_{s,on}{}'}{N_{s,off}{}'}\right)$.However, because the spectral purity is not 100%, but it only is ξ, the relationship between the two channel signals is approximately $N_{s,on} = N_{s,off}[(1-\xi) + \xi e^{-2dOD}]$, $ln\left(\frac{N_{s,on}}{N_{s,off}}\right) = ln[(1-\xi) + \xi e^{-2dOD}]$, and the spectral purity yield the following error in optical depth:

$$\varepsilon_\xi = \frac{1}{2} ln\left(\frac{N_{s,on}}{N_{s,off}}\right) - \frac{1}{2} ln\left(\frac{N_{s,on}{}'}{N_{s,off}{}'}\right)$$

$$\approx dOD + \frac{1}{2} ln[1 - \xi(1 - e^{-2dOD})] \qquad (38)$$

https://doi.org/10.5194/amt-2022-69
Preprint. Discussion started: 25 April 2022

Atmospheric Measurement Techniques Discussions

Table 10 Error in differential optical depth from spectral purity of 99.99%

Wavelength	*dOD*(0, 71km)	*Error* (spectral purity of 99.99%)
764.6840 764.9097	0.428	6.79×10^{-5}
765.1600 764.9707	0.325	4.60×10^{-5}
765.1736 765.3883	0.328	4.66×10^{-5}
765.6735 765.4637	0.192	2.36×10^{-5}
759.8042 759.4629	0.493	8.40×10^{-5}
759.8969 759.4629	0.322	4.51×10^{-5}
760.0209 759.4629	0.364	5.35×10^{-5}
760.1674 759.4629	0.484	8.16×10^{-5}
760.3133 759.4629	0.554	1.01×10^{-4}

3.3.8 Error of differential optical depth caused jitter of *v* in central optical frequency

The laser source of the spaceborne IPDA has a jitter of v central optical frequency, whereas the online/offline emission laser spectrum has a central frequency jitter of 10MHz(Strotkamp et al., 2019).$\Delta v_{on}=\pm$ 10MHz introduces uncertainty in the Oxygen molecule absorption cross-section σ (v_{on}), resulting in a systematic error in the optical depth. However, for solid-state lasers, stabilizing the center wavelength within ±10MHz is quite easy compared to within ±1MHz. For example, if the center wavelength is offset by ±10MHz, the jitter of the emitted laser frequency that affects the swing of the optical depth can be expressed as

$$[dOD(0,surface)]_{10MHZ}=\int_0^{71km}\frac{0.20948p(z)}{kT(z)\big(1+\chi(z)\big)}\Big(\sigma(v_{on}\pm10MHZ,z)-\sigma\big(v_{off},z\big)\Big)dz$$

$$-\int_0^{71km}\frac{0.20948p(z)}{kT(z)(1+\chi(z))}\Big(\sigma(v_{on},z)-\sigma\big(v_{off},z\big)\Big) \quad (39)$$

It is evident from the curves of the two bands in Fig.5 that because the former is next to an absorption line 13069.062119cm^{-1} of the oxygen isotope $^{16}O^{18}O$, the curvature at the former position protrudes, and the abscissa of the curve is the laser frequency (Wavelength).

Table 11 Jitter in the emission laser frequency v causes a 10MHz change in the differential optical depth

https://doi.org/10.5194/amt-2022-69
Preprint. Discussion started: 25 April 2022

Atmospheric Measurement Techniques Discussions

λ(nm)	*dOD* (v±10MHZ, p)- *dOD* (v, p)		Max{│Δ(+10MHz)│,│Δ(-10MHz)│}
	│Δ(+10MHz)│	│Δ(-10MHz)│	
764.6840 / 764.9097	6.18 $\times 10^{-7}$	9.62 $\times 10^{-7}$	9.62 $\times 10^{-7}$
765.1600 / 764.9707	2.23 $\times 10^{-5}$	2.38 $\times 10^{-5}$	2.38 $\times 10^{-5}$
765.1736 / 765.3883	2.00 $\times 10^{-6}$	2.81$\times 10^{-6}$	2.81$\times 10^{-6}$
765.6735 / 765.4637	1.04 $\times 10^{-6}$	8.53 $\times 10^{-7}$	1.04 $\times 10^{-6}$
759.8042 / 759.4629	4.28 $\times 10^{-3}$	2.52$\times 10^{-3}$	4.28 $\times 10^{-3}$
759.8969 / 759.4629	1.56 $\times 10^{-3}$	1.19 $\times 10^{-3}$	1.56 $\times 10^{-3}$
760.0209 / 759.4629	7.71 $\times 10^{-4}$	7.76$\times 10^{-4}$	7.76 $\times 10^{-4}$
760.1674 / 759.4629	6.84$\times 10^{-4}$	1.60 $\times 10^{-3}$	1.60 $\times 10^{-4}$
760.3133 / 759.4629	3.83 $\times 10^{-4}$	9.49 $\times 10^{-4}$	9.49 $\times 10^{-4}$

According to the comprehensive analysis of the above differential optical depth errors induced in many factors, the comprehensive evaluation index items of the wavelength to be selected are shown in Figure 12 and Figure 13.

Table 12 Comprehensive of various errors at near 765nm

Wavelength		764.6840 /764.9097	765.1600 /764.9707	765.1736 /765.3883	765.6735 /765.4637
Random error	ocean	2.44 $\times 10^{-4}$	2.24 $\times 10^{-4}$	2.20 $\times 10^{-4}$	2.00 $\times 10^{-4}$
	land	3.55$\times 10^{-4}$	3.30$\times 10^{-4}$	3.24 $\times 10^{-4}$	2.96 $\times 10^{-4}$
Temperature	1K	21.54 $\times 10^{-4}$	9.31 $\times 10^{-4}$	10.16$\times 10^{-4}$	1.43 $\times 10^{-4}$
Vapor mixing ratio	20%	5.29 $\times 10^{-4}$	4.15 $\times 10^{-4}$	4.18 $\times 10^{-4}$	2.53$\times 10^{-4}$
Energy monitor channel calibration		1.07 $\times 10^{-4}$	0.813 $\times 10^{-4}$	0.820 $\times 10^{-4}$	0.480 $\times 10^{-4}$
Echo channel calibration		1.07 $\times 10^{-4}$	0.813 $\times 10^{-4}$	0.820 $\times 10^{-4}$	0.480 $\times 10^{-4}$

https://doi.org/10.5194/amt-2022-69
Preprint. Discussion started: 25 April 2022

Elevation 2m error	0.458×10^{-4}	0.372×10^{-4}	0.374×10^{-4}	0.236×10^{-4}
Aerosol Mie scattering	0.903×10^{-4}	0.756×10^{-4}	0.857×10^{-4}	0.837×10^{-4}
99.99% spectral purity	0.679×10^{-4}	0.460×10^{-4}	0.466×10^{-4}	0.236×10^{-4}
Frequency jitter(10MHZ)	9.62×10^{-7}	0.238×10^{-4}	2.81×10^{-6}	1.04×10^{-6}
Differential absorption cross section (m^2)	1.80×10^{-29}	1.46×10^{-29}	1.47×10^{-29}	9.25×10^{-30}
Geometrically added	25.8×10^{-4}	19.6×10^{-4}	14.3×10^{-4}	6.08×10^{-4}
Absolute error(hPa)	3.29	3.08	2.23	1.51
Relative error(%)	0.324	0.304	0.220	0.150

Table 13 Comprehensive of various errors at near 760nm

Wavelength		759.8042 /759.4629	759.8969 /759.4629	760.0209 /759.4629	760.1674 /759.4629	760.3133 /759.4629
Random error	ocean	2.59×10^{-4}	2.09×10^{-4}	2.22×10^{-4}	2.64×10^{-4}	2.96×10^{-4}
	land	3.78×10^{-4}	3.06×10^{-4}	3.25×10^{-4}	3.84×10^{-4}	4.29×10^{-4}
Temperature	1K	26.2×10^{-4}	4.64×10^{-4}	9.10×10^{-4}	27.5×10^{-4}	47.8×10^{-4}
Vapor mixing ratio	20%	7.68×10^{-4}	4.86×10^{-4}	5.38×10^{-4}	7.03×10^{-4}	7.95×10^{-4}
Energy monitor channel calibration		1.91×10^{-4}	1.25×10^{-4}	1.40×10^{-4}	1.96×10^{-4}	2.28×10^{-4}
Echo channel calibration		1.91×10^{-4}	1.25×10^{-4}	1.40×10^{-4}	1.96×10^{-4}	2.28×10^{-4}
Elevation 2m error		0.22×10^{-4}	0.14×10^{-4}	0.16×10^{-4}	0.22×10^{-4}	0.26×10^{-4}
Aerosol Mie scattering		1.21×10^{-4}	1.59×10^{-4}	2.09×10^{-4}	2.69×10^{-4}	3.29×10^{-4}
99.99% spectral purity		0.840×10^{-4}	0.451×10^{-4}	0.535×10^{-4}	0.816×10^{-4}	1.01×10^{-4}
Frequency jitter(10MHZ)		42.8×10^{-4}	15.6×10^{-4}	7.76×10^{-4}	16.0×10^{-4}	9.49×10^{-4}
Differential absorption cross section (m^2)		2.45×10^{-29}	1.51×10^{-29}	1.63×10^{-29}	2.08×10^{-29}	2.32×10^{-29}
Geometrically added		54.6×10^{-4}	20.2×10^{-4}	16.7×10^{-4}	36.7×10^{-4}	53.9×10^{-4}
Absolute error(hPa)		5.12	3.07	2.35	4.05	5.34
Relative error(%)		0.505	0.302	0.232	0.400	0.527

Consequently, according to Table 12 and Table 13, the pulse energy, pulse repetition, time resolution, and distance along track are 100mJ, 100Hz, 6.25 s, and 44km, respectively. The 765.6735/765.4637 wavelength pairs are used as detection wavelength and reference wavelength. In the 1K error temperature profile, 20% error vapor mixing ratio result in 6.08×10^{-4} error in differential optical depth, which corresponds to an absolute error in surface pressure of 1.51hPa, therefore, it is a desirable result that the relative error of surface pressure could be considered as 0.150%.

https://doi.org/10.5194/amt-2022-69
Preprint. Discussion started: 25 April 2022

Atmospheric Measurement Techniques
Discussions

4 Summary

The calculation process of retrieving the surface pressure from the atmospheric differential optical depth was also discussed. The performance of the differential absorption LIDAR model was evaluated. Owing to the influence of temperature on Oxygen absorption coefficient and the uncertainty of atmospheric mixing ratio, maintaining the relative error of surface atmospheric pressure below 0.1% is a challenging task. The main factors affecting the random error of surface pressure are the low sea reflectivity, random error of low signal-to-noise ratio, and the uneven ground, which renders the multi pulse echo unable to be accumulated and averaged directly. Further, 765.6735/765.4637nm was selected as the working wavelength, the pulse energy, pulse repetition, time resolution, distance along the track resolution are 100mJ, 100Hz, 6.25 s, and 44km, respectively, while the relative error of surface atmospheric pressure was controlled in the range of 0.2–0.3%.

Author contribution

Guanglie Hong developed the model and Yu Dong performed the simulations,was responsible for data processing and software code. Guanglie Hong provided part of the manuscript and analyzed the method respectively. Huige Di supervised and modified the manuscript.

Competing interests

I declare that there is no conflict of interest.

References

Brown, R. A. and Levy, G.: Ocean surface pressure fields from satellite-sensed winds, Mon. Wea. Rev.114, doi.org/10.1175/1520-0493, 1986.

Korb, C. L., Schwemmer, G. K., Famiglietti, J., Walden, H. and Prasad, C.: Differential Absorption LIDARS for Remote Sensing of Atmospheric Pressure and Temperature Profiles: Final Report, NASA Tech. Memo. 104618, 1995.

Korb, C. L. and Weng, C. Y.: Differential absorption LIDAR technique for measurement of the atmospheric pressure profile, Appl.Opt.22(23), 3759-3770, doi:10.1364/AO.22.003759, 1983.

Schwemmer, G. K., Dombrowski, M., Korb, C. L. Milrod, J., Walden, H. and Kagann, R. H.: A LIDAR system for measuring atmospheric pressure and temperature profiles, Rev. Sci. Instrum.58(12), 2226~2237, doi:10.1063/1.1139327, 1987.

Korb, C. L., Schwemmer, G. K., Dombrowski, M. and Weng, C. Y.: Airborne and ground based LIDAR measurements of the atmospheric pressure profile, Appl.Opt.28(15), 3015~3020, doi:10.1364/AO.28.003015, 1989.

Flamant, C. N., Schwemmer, G. K., Korb, C. L., Evans, K. D. and Palm, S. P.: Pressure Measurements using and Airborne Differential Absorption LIDAR. Part I: Analysis of the Systematic Error Sources, J. Atmos. and Ocean. Technol.16,561~574, doi:http://dx.doi.org/10.1175/1520-0426(1999)0162.0.CO;2, 1999.

https://doi.org/10.5194/amt-2022-69
Preprint. Discussion started: 25 April 2022

Zaccheo,T.S., Pernini,T., Snell, H. E. and Browell, E. V.: Impact of atmospheric state uncertainties on retrieved XCO2 columns from laser differential absorption spectroscopy measurements, Journal of Applied remote sensing, 083575, doi:10.1117/1.jrs.8.083575, 2014.

Crowell, S., Rayner, P., Zaccheo, S. and Moore, B.: Impacts of atmospheric state uncertainty on O_2 measurement requirements for the ASCENDS mission, Atmos. Meas. Tech.,8, 2685-2697, doi:10.5194/amt-8-2685-2015, 2015.

Stephen, M. A., Krainak, M., Riris, H. and Allan, G. R.: Narrowband, tunable, frequency-doubled, erbiumdoped fiber-amplifed transmitter, Opt. Lett.32, 2073-2075, doi:10.1364/OL.32.002073, 2007.

Stephen, M. A., Mao, J. P., Abshire, J. B., Sun, X., Kawa, S. R. and Krainak, M. A.: Oxygen Spectroscopy Laser Sounding Instrument for Remote Sensing of Atmospheric Pressure, OSA, doi:10.1109/aero.2008.4526388, 2008.

Riris, H., Rodriguez, M., Allan, G. R., Hasselbrack, W. E., Stephen, M. A. and Abshire, J. B.: Airborne LIDAR measurements of atmospheric pressure made using the oxygen A-band, Lasers, Sources, and Related Photonic Devices Technical Digest, OSA, doi:10.1117/12.892021, 2012.

Riris, H., Rodriguez, M., Allan, G. R., Hasselbrack, W. E., Mao, J. P., Stephen, M.A. and Abshire, J.: Pulsed airborne LIDAR measurements of atmospheric optical depth using the Oxygen A-band at 765nm, Appl. Opt.52(25), 6369-6382, doi:10.1364/ao.52.006369, 2013.

Riris, H., Rodriguez, M., Mao, J. P., Allan, G. and Abshire, J.: Airborne demonstration of atmospheric oxygen optical depth measurements with an integrated path differential absorption LIDAR, Opt.Express25(23) 29307~29327, doi:10.1364/oe.25.029307, 2017.

Millán, L., Lebsock, M., Livesey, N., Tanelli,S. and Stephens, G.: Differential absorption radar techniques: surface pressure, Atmos. Meas. Tech.7, 3959-3970, doi:10.5194/amt-7-3959-2014, 2014.

Brown, L. R. and Plymate, C.: Experimental Line Parameters of the Oxygen A Band at 760 nm, J. Mol. Spectrosc.199, 166-179, doi:10.1006/jmsp.1999.8012, 2000.

Munk, A., Jungbluth, B., Strotkamp, M., Hoffmann, H.-D., Poprawe, R., Höffner, J. and Lübken, F.-J.: Diode-pumped alexandrite ring laser in single-longitudinal mode operation for atmospheric LIDAR measurements, Opt.Express26(12), 14928-14935， doi: 10.1364/oe.26.014928， 2018

Munk, A., Strotkamp, M., Walochnik, M., Jungbluth, B., Traub, M., Hoffmann, H. -D., Poprawe, R., Höffner, J. and Lübken, F.-J.: Diode-pumped Q-switched Alexandrite laser in single longitudinal mode operation with Watt-level output power, Opt. Lett.43(22), 5492-5495, doi:10.1364/OL.43.005492, 2018.

https://doi.org/10.5194/amt-2022-69
Preprint. Discussion started: 25 April 2022

Coney, A. T. and Damzen, M. J.: High-energy diode-pumped alexandrite amplifier development with applications in satellite-based LIDAR, Journal of the Optical Society of America B38(1), 209-219, doi:10.1364/JOSAB.409921, 2021.

Strotkamp, M., Munk, A., Jungbluth, B., Hoffmann, H. D. and Hoffner, J.: Diode pumped Alexandrite laser for next generation satellite based earth observation LIDAR, CEAS Space J.11, 413-422, doi:10.1007/s12567-019-00253-z, 2019.

Munk, A., Jungblutha, B., Strotkamp, M., Hoffmann, H.-D., Poprawe, R. and Höffner, J.: Alexandrite laser in Q-switched, single longitudinal mode operationpumped by a fiber-coupled diode module, Proc. SPIE 10896,1089610, doi:10.1117/12.2508402, 2019.

Munk, A., Jungbluth, B., Strotkamp, M., Hoffmann, H.-D., Poprawe, R. and Höffner, J.: Diode-pumpedAlexandrite ring laser for LIDAR applications," Proc. SPIE 9726, 97260I, doi:10.1117/12.2212578, 2016.

Thomas, G. M., Minassian, A., Sheng, X. and Damzen, M. J.: Diode-pumped Alexandrite lasers in Q-switchedand cavity-dumped Q-switched operation, Opt. Express24(24), 27212–27224, doi:10.1364/OE.24.027212, 2016.

Wulfmeyer, V. and ¨osenberg, J. B.: Single-mode operation of an injection-seededalexandrite ring laser for application in water-vapor and temperature differential absorption LIDAR, Opt. Lett.21(15), 1150-1152, doi:10.1364/OL.21.001150, 1996.

Lemmerz, C., Lux, O., Reitebuch, O., Witschas, B. and Wührer, C.: Frequency and timing stability of an airborneinjection-seeded Nd:YAG laser system fordirect-detection wind LIDAR, Appl. Opt.56(32), 9057-9068, doi:10.1364/AO.56.009057, 2017.

Lancaster, R. S., Spinhirne, J. D. and Palm, S. P.: Laser pulse reflectance of the ocean surface from the GLAsatellite LIDAR, Geophys. Res. Lett.32, L22S10, doi:10.1029/2005GL023732, 2015.

Bufton, J. L., Hoge, F. E. and Swift, R. N.: Airborne measurements of laser backscatter from the ocean surface, Appl. Opt.22(17)，2603- 2618, doi:10.1364/AO.22.002603, 1983.

Menzies, R. T., Tratt, D. M. and Hunt, W. H.: LIDAR In-space Technology Experiment measurements of sea surface directional reflectance and the link to surface wind speed, Appl. Opt.37(24)，5550-5559, doi:10.1364/AO.37.005550, 1998.

Ehret, G., Kiemle,C., Wirth, M., Amediek, A., Fix, A. and Houweling, S.: Space-borne remote sensing of CO2, CH4,and N2O by integrated path differential absorption LIDAR: a sensitivity analysis, Appl. Phys. B 90, 593–608, doi:10.1007/s00340-007-2892-3, 2008.

Standard solar constant and zero air mass solar spectral irradiance tables, ASTM international, 100 BrrHarbor Drive, United States, 2000.

https://doi.org/10.5194/amt-2022-69
Preprint. Discussion started: 25 April 2022

Atmospheric Measurement Techniques Discussions

Refaat, T. F., Ismail, S., Nehrir, A. R., Hair, J.W., Crawford, J. H., Leifer, I. and Shuman, T.: Performance evaluation of a 1.6-µm methane DIAL system from ground, aircraft and UAV platforms, Opt. Express21(25), 30415-30432, doi:10.1364/OE.21.030415, 2013.